Journal of Materials Chemistry A

PAPER

Cite this: J. Mater. Chem. A, 2017, 5, 18261

Hydrogen evolution reaction catalyzed by ruthenium ion-complexed graphitic carbon nitride nanosheets†

Yi Peng,[a] Bingzhang Lu,[a] Limei Chen,[a] Nan Wang,[b] Jia En Lu,[a] Yuan Ping*[a] and Shaowei Chen*[a]

The development of cost-effective, high-performance electrocatalysts for hydrogen evolution reaction (HER) is urgently needed. In the present study, a new type of HER catalyst was developed where ruthenium ions were embedded into the molecular skeletons of graphitic carbon nitride (C_3N_4) nanosheets of 2.0 ± 0.4 nm in thickness by refluxing C_3N_4 and $RuCl_3$ in water. This took advantage of the strong affinity of ruthenium ions to pyridinic nitrogen of the tri-*s*-triazine units of C_3N_4. The formation of C_3N_4–Ru nanocomposites was confirmed by optical and X-ray photoelectron spectroscopic measurements, which suggested charge transfer from the C_3N_4 scaffold to the ruthenium centers. Significantly, the hybrid materials were readily dispersible in water and exhibited apparent electrocatalytic activity towards HER in acid and their activity increased with the loading of ruthenium metal centers in the C_3N_4 matrix. Within the present experimental context, the sample saturated with ruthenium ion complexation at a ruthenium to pyridinic nitrogen atomic ratio of *ca.* 1 : 2 displayed the best performance, with an overpotential of only 140 mV to achieve the current density of 10 mA cm^{-2}, a low Tafel slope of 57 mV dec^{-1}, and a large exchange current density of 0.072 mA cm^{-2}. The activity was markedly lower when C_3N_4 was embedded with other metal ions such as Fe^{3+}, Co^{3+}, Ni^{3+} and Cu^{2+}. This suggests minimal contributions from the C_3N_4 nanosheets to the HER activity, and the activity was most likely due to the formation of Ru–N moieties where the synergistic interactions between the carbon nitride and ruthenium metal centers facilitated the adsorption of hydrogen. This was strongly supported by results from density functional theory calculations.

Received 3rd May 2017
Accepted 31st July 2017

DOI: 10.1039/c7ta03826g

rsc.li/materials-a

Introduction

Electrochemical water splitting for hydrogen generation represents an attractive technology for electrochemical energy storage and conversion.[1–3] Mechanistically, hydrogen evolution reaction (HER) involves multiple electron-transfer processes and requires appropriate catalysts to achieve a fast hydrogen evolution rate.[4–7] Until now, carbon-supported Pt has been recognized as the leading catalyst for HER with a high exchange-current density and a small Tafel slope.[8] However, the high costs of Pt have severely hampered its wide-spread application. Thus, the development of non-platinum HER catalysts as cost-effective alternatives has been attracting a great deal of attention. For instance, transition metal sulfides, nitrides, phosphides, carbides and oxides (MX, with M = Mo, Fe, Co, Ni, *etc.*) have been found to exhibit apparent activity towards HER.[9–17] However, because of their low dispersibility in water, their catalytic activity is limited by the accessibility of the active centers. In addition, their durability may be compromised due to structural instability of the catalysts at low pH, a typical condition for HER.

In contrast, for homogeneous catalysts based on organometallic complexes, such as cobalt macrocyclic glyoxime and tetraimine complexes,[18] cobalt and nickel diimine–dioxime complexes,[19] copper phthalocyanine complexes,[20] and ruthenium complexes,[21] surface accessibility is markedly enhanced. In these catalysts, the metal centers are coordinated to nitrogen-containing organic ligands, and the resulting M–N_x moieties are generally believed to serve as the active sites for HER catalysis. Yet, despite much progress, their HER performance has remained largely subpar as compared to those of state-of-the-art platinum catalysts.[22]

Herein, by taking advantage of the abundant pyridinic nitrogen moieties in graphitic carbon nitride (C_3N_4) nanosheets, we embedded ruthenium ions within the C_3N_4 molecular skeleton forming Ru–N_x bonds that may serve as effective

[a]Department of Chemistry and Biochemistry, University of California, 1156 High Street, Santa Cruz, CA 95064, USA. E-mail: shaowei@ucsc.edu; yuanping@ucsc.edu
[b]New Energy Research Institute, School of Environment and Energy, South China University of Technology, Guangzhou High Education Mega Centre, Guangzhou, Guangdong 510006, China

† Electronic supplementary information (ESI) available: Additional experimental and computational data. See DOI: 10.1039/c7ta03826g

active sites for HER, analogous to conventional organometallic complexes. Owing to its high chemical/thermal stability,[23–34] C_3N_4 has been explored as an advanced metal-free catalyst for a variety of energy conversion/storage processes.[35,36] For instance, C_3N_4-based materials have been used as effective photocatalysts where the electronic band gap structure may be readily manipulated by doping with non-metal elements.[37–42] However, applications of C_3N_4 in electrocatalysis, such as HER, have been limited by its low electrical conductivity. This may be mitigated by the incorporation of metal ions into the C_3N_4 molecular skeleton by taking advantage of the tri-*s*-triazine units of C_3N_4 that readily chelate transition metal ions.

Experimentally, the successful incorporation of ruthenium metal ions into the C_3N_4 matrix was manifested by the emergence of unique metal–ligand charge transfer (MLCT) in UV-vis and photoluminescence (PL) measurements. XPS measurements suggested electron transfer from the C_3N_4 skeleton to the ruthenium metal centers. Remarkably, the C_3N_4–Ru nanocomposites were found to be readily dispersed in water and exhibit apparent HER activity in acid, which increased with increasing loading of the ruthenium metal centers. Within the present experimental context, the sample saturated with ruthenium complexation at a ruthenium to pyridinic nitrogen ratio of *ca.* 1 : 2 displayed the best performance, with a low overpotential of only 140 mV to achieve the current density of 10 mA cm^{-2}, a small Tafel slope of 57 mV dec^{-1}, and a large exchange current density of 0.072 mA cm^{-2}, which was superior/comparable to results reported recently with C_3N_4-based HER catalysts. This remarkable performance was due to the formation of Ru–N moieties where the synergistic interactions between pyridinic nitrogen and ruthenium metal centers facilitated the adsorption of protons with a decrease of the Gibbs free energy. In fact, control experiments with other transition metal ions such as Fe^{3+}, Co^{3+}, Ni^{3+} and Cu^{2+} showed only minimal contributions from the C_3N_4 nanosheets to the HER activity, and studies based on DFT calculations showed a downshift of the valence and conduction bands of C_3N_4 and enhancement of electron mobility after embedment of ruthenium ions into the C_3N_4 matrix. This led to optimized proton adsorption and reduction of the Gibbs free energies due to delocalized electrons from the ruthenium centers.

Experimental section

Chemicals

Melamine (99%, Acros), ruthenium(III) chloride ($RuCl_3$, 35–40% Ru, Acros), ruthenium(IV) oxide (RuO_2, 99.5%, anhydrous, ACROS), copper(II) acetate monohydrate ($Cu(OAc)_2 \cdot H_2O$, +98%, Alfa Aesar), cobalt(II) acetate tetrahydrate ($Co(OAc)_2 \cdot 4H_2O$, +99%, Matheson Coleman & Bell), nickel(II) acetate tetrahydrate, ($Ni(OAc)_2 \cdot 4H_2O$, +99%, Matheson Coleman & Bell), iron(II) chloride tetrahydrate ($FeCl_2 \cdot 4H_2O$, +99%, Fisher Scientific), and sulfuric acid (98%, Fisher Chemicals) were used as received. All solvents were obtained from typical commercial sources and used without further treatment. Water was supplied by a Barnstead Nanopure water system (18.3 MΩ cm).

Material preparation

Graphitic C_3N_4 nanosheets were synthesized by thermal treatment of melamine in air, as detailed previously.[43,44] Briefly, 10 g of melamine was placed in a ceramic crucible with a cover and heated to 600 °C at a heating rate of 2.3 °C min^{-1}. The sample was heated at this temperature for 3 h before being cooled down to room temperature, yielding a yellow product that was ground to fine powders. To synthesize ruthenium ion-complexed carbon nitride (C_3N_4–Ru), 50 mg of the C_3N_4 powders synthesized above were first dispersed into 50 mL of nanopure H_2O under sonication overnight to produce C_3N_4 thin layers. 56 mg of $RuCl_3$ was then added to the mixture, which was refluxed for 4 h. The product was collected by centrifugation at 4500 rpm for 10 min and washed with nanopure H_2O and ethanol to remove excess ruthenium ions. Note that in this synthesis, the supernatant showed a light brown color, indicating that there was a small excess of ruthenium ions in the solution and C_3N_4 was saturated with ruthenium complexation. The corresponding sample was referred to as C_3N_4–Ru–F. Another sample was prepared in the same manner except the amount of $RuCl_3$ added was reduced by half to 28 mg. After centrifugation, the supernatant was colorless, indicating that all ruthenium ions were incorporated into C_3N_4. The product was denoted as C_3N_4–Ru–P.

C_3N_4 complexed with other transition-metal ions (*i.e.*, Fe^{3+}, Co^{3+}, Ni^{3+} and Cu^{2+}) was also prepared in a similar fashion where an equivalent amount of the salt precursors was used instead of $RuCl_3$, and the corresponding products were referred to as C_3N_4–Fe, C_3N_4–Co, C_3N_4–Ni, and C_3N_4–Cu. For these samples, the supernatants after centrifugation showed the same colors as those of the original metal salts, suggesting that the metal ions were in excess and C_3N_4 was saturated with the respective metal ions.

Characterization

Transmission electron microscopic (TEM) measurements were performed with a JEOL JEM 2100F microscope. Atomic force microscopic (AFM) measurements were carried out with a Molecular Imaging PicoLE SPM instrument. X-ray diffraction (XRD) patterns were acquired with a Rigaku Americas Miniflex Plus powder diffractometer operated at the voltage of 40 kV and current of 30 mA. XPS measurements were carried out with a PHI 5400/XPS instrument equipped with an Al K_α source operated at 350 W and 10^{-9} Torr. UV-vis spectra were collected with a Perkin Elmer Lambda 35 UV-vis spectrometer, and PL measurements were performed with a PTI fluorospectrometer. Inductively coupled plasma mass spectrometric (ICP-MS) analysis was carried out with an Agilent 1260-7700e instrument.

Electrochemistry

Electrochemical tests were performed using a CHI710 workstation and electrochemical impedance measurements were carried out with a Gamry Reference 600 instrument. A Ag/AgCl electrode (saturated KCl) and Pt wire were used as the reference electrode and counter electrode, respectively, while

a glassy carbon electrode (5 mm in diameter, 0.196 cm^2) was used as the working electrode. The Ag/AgCl electrode was calibrated against a reversible hydrogen electrode (RHE) and all the potentials were referenced to this RHE electrode. To prepare catalyst inks, 2 mg of the C_3N_4–M powders obtained above and 3 mg of carbon black were dispersed in 1 mL of 1 : 4 (v/v) water/ethanol mixed solvents along with 10 μL of a Nafion solution, and the mixture was sonicated for 30 min to achieve good dispersion of the materials. Then 15 μL of the inks was drop cast onto the surface of the glassy carbon electrode and dried at room temperature, corresponding to a mass loading of 0.153 mg cm^{-2} for the catalysts.

Full water splitting was carried out with C_3N_4–Ru–F as the HER catalyst and commercial RuO_2 as the catalyst for the oxygen evolution reaction (OER), along with a Ag/AgCl reference electrode. To prepare the electrodes, the catalysts were dispersed in ethanol at a concentration of 2 mg mL^{-1} under sonication for 0.5 h; then 0.5 mL of the catalyst inks was drop cast onto a piece of carbon cloth (1 cm × 2 cm) yielding a mass coverage of 0.5 mg cm^{-2}. Water splitting tests were performed with an applied potential of 2 V in 1 M KOH, and the amounts of hydrogen and oxygen generated were quantified by water displacement measurements.

DFT calculations

The calculations of the electronic structures of C_3N_4 and C_3N_4–Ru were carried out by using open-source plane wave code, Quantum Espresso.[45] The two-dimensional unit cell was built with two chemical formulae of C_3N_4 and one Ru atom. The interlayer distance was set at 20 Å so that there was no interaction between the layers. The ultrasoft pseudo-potential[46] was adopted with the wave function cutoff of 40 Ry (charge density cutoff 200 Ry), the energy threshold at 10^{-8} Ry, and the force converged to 10^{-4} a.u. The Marzari–Vanderbilt smearing[47] was adopted with 0.01 Ry for C_3N_4–Ru since the system became metal-like. We used 4 × 4 × 1 uniform *k* point mesh to sample the first Brillouin zone. The vibrational frequencies of surface species, zero-point energy (ZPE) and entropy contribution were evaluated by density functional perturbation theory (DFPT).[48] All atoms were initiated with spin polarization. The structural model details and Gibbs free-energy calculations are included in the ESI.†

Results and discussion

C_3N_4 nanosheets were synthesized by thermal treatment of melamine in air,[43,44] and refluxing with $RuCl_3$ in water led to effective incorporation of ruthenium metal ions into the C_3N_4 scaffolds, most likely forming Ru–N_x moieties through the pyridinic nitrogen, as schematically shown in Fig. 1A. Fig. 1B depicts a typical TEM image of the C_3N_4–Ru–F sample where nanosheet structures of a few tens of nm can be readily identified, rather consistent with the as-prepared C_3N_4 (Fig. S1†). In XRD measurements (Fig. S2†), both C_3N_4–Ru–F and the as-prepared C_3N_4 nanosheets displayed a single diffraction peak centered at 27.2°, corresponding to an interplanar spacing of 0.326 nm that

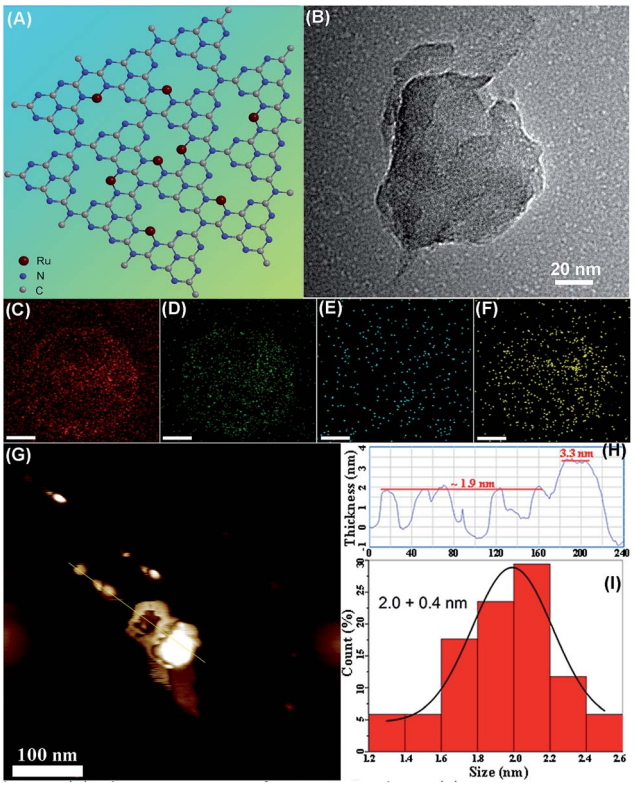

Fig. 1 (A) Schematic structure of C_3N_4–Ru nanosheets. (B) Representative TEM image of C_3N_4–Ru–F. EDX images of various elements in C_3N_4–Ru–F (scale bars all 50 nm): (C) C, (D) N, (E) Ru, and (F) Cl. (G) Representative AFM topograph of C_3N_4–Ru–F (scale bar 100 nm). (H) Height profile of the line scan in panel (G). (I) Histogram of the thickness of C_3N_4–Ru–F nanosheets based on the AFM topographic measurements.

is characteristic of the C_3N_4 (002) planes.[37,41,49] Energy dispersive X-ray (EDX) measurements confirmed that indeed Ru ions were incorporated into the C_3N_4 matrix, as manifested in the elemental maps of C, N, Ru and Cl in Fig. 1C–F, which were all distributed rather evenly across the sample.

A representative AFM topograph is depicted in Fig. 1G, and the height profile of a line scan is shown in Fig. 1H, where the thickness of the C_3N_4–Ru nanosheets was found to be rather consistent at *ca.* 2 nm. In fact, statistical analysis based on more than 100 nanosheets showed that the average thickness was 2.0 ± 0.4 nm, as manifested in the thickness histogram (Fig. 1I), identical to that of the as-produced C_3N_4 nanosheets (Fig. S3†).

XPS measurements were then carried out to determine the chemical composition and valence states of the composites. Fig. 2A depicts the survey spectra of (i) C_3N_4, (ii) C_3N_4–Ru–P and (iii) C_3N_4–Ru–F, where the C 1s and N 1s electrons can be readily identified at *ca.* 285 eV and *ca.* 399 eV for all samples, and both C_3N_4–Ru–F and C_3N_4–Ru–P also exhibited two additional peaks at *ca.* 282 eV and *ca.* 199 eV, due to Ru 3d and Cl 2p electrons, respectively. The high-resolution scan of the Cl 2p electrons is depicted in Fig. 2B where the binding energy was found to peak at 197.50 (Cl $2p_{3/2}$) and 199.00 eV (Cl $2p_{1/2}$) for C_3N_4–Ru–P and 197.70 (Cl $2p_{3/2}$) and 199.20 eV (Cl $2p_{1/2}$) for C_3N_4–Ru–F, consistent with those of Cl^- ions in outer-sphere.[50,51] The C 1s

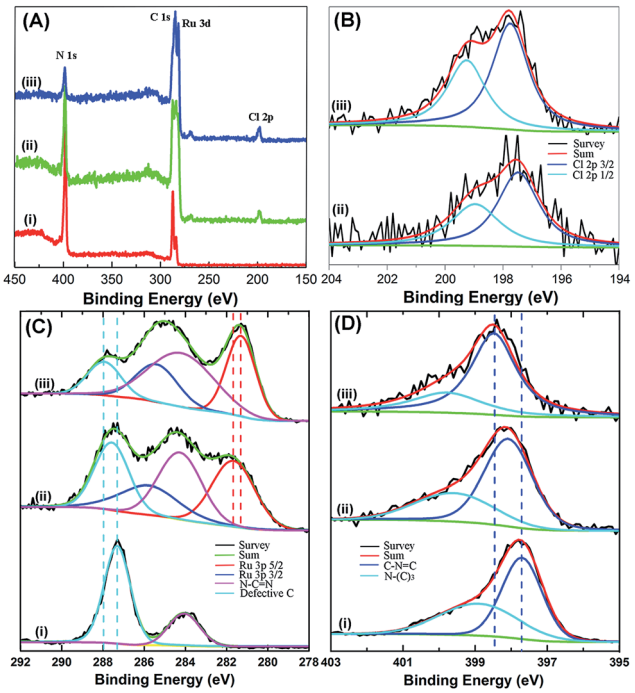

Fig. 2 (A) XPS survey spectra of (i) C_3N_4, (ii) C_3N_4–Ru–P, and (iii) C_3N_4–Ru–F. High-resolution XPS spectra of (B) Cl 2p, (C) C 1s and Ru 3d, and (D) N 1s electrons. Black curves are experimental data and colored curves are deconvolution fits.

and Ru 3d spectra are depicted in Fig. 2C. For the as-prepared C_3N_4, the C 1s spectrum can be deconvoluted into two peaks, a major one at 287.31 eV and a minor one at 284.06 eV. The former may be assigned to the sp^2-hybridized carbon in N–C=N of the C_3N_4 matrix, while the latter likely arose from defective carbon in sp^3 C–C bonds.[31,32] Interestingly, the binding energy of C 1s in N–C=N blue-shifted somewhat to 287.57 eV for C_3N_4–Ru–P and even further to 287.93 eV for C_3N_4–Ru–F, likely due to the binding of (positively charged) ruthenium ions to the nitrogen moiety. For the Ru 3d electrons, the doublet can be resolved at 281.67 eV (Ru $3d_{5/2}$) and 285.77 eV (Ru $3d_{3/2}$) for C_3N_4–Ru–P, and slightly lower at 281.30 eV (Ru $3d_{5/2}$) and 285.40 eV (Ru $3d_{3/2}$) for C_3N_4–Ru–F. Note that these binding energies are actually close to those of Ru(II) 3d electrons in a ruthenium tris-bipyridine complex,[52] indicating that ruthenium was reduced to +2 from the original +3 charge state likely by hydroxide species, as observed previously by Creutz and Sutin,[53] and incorporated into the C_3N_4 matrix by Ru–N coordination bonds that enhanced electron-withdrawing of the nitrogen atoms. In fact, consistent results can be obtained in the high-resolution scans of the N 1s electrons (Fig. 2D). For the C_3N_4 nanosheets, two peaks were resolved, a major one at 397.80 eV that may be attributed to the sp^2-hybridized pyridinic nitrogen (C–N=C) and a minor one at 399.58 eV that can be assigned to the sp^3-hybridized tertiary nitrogen (N–$(C)_3$). After ruthenium ion complexation, the C–N=C peak blue-shifted to 398.08 eV for C_3N_4–Ru–P and 398.48 eV for C_3N_4–Ru–F (whereas the N–$(C)_3$ peak remained almost invariant). Note that in a previous study,[54] the N 1s binding energy of a polypyridyl ligand was also found to exhibit a positive shift of *ca.* 0.3 eV upon complexation with Ru(II) ions. These observations suggest charge transfer from the C_3N_4 skeleton to the Ru d-orbital. Such MLCT may have significant implication in the electrocatalytic activity (*vide infra*).

Furthermore, based on the integrated peak areas, the elemental compositions of the samples were then analyzed. First, the atomic ratio of C(N–C=N) : N was estimated to be 1 : 1.27 for C_3N_4, 1 : 1.20 for C_3N_4–Ru–P, and 1 : 1.18 for C_3N_4–Ru–F, in good agreement with the expected value of 1 : 1.33. In addition, the Ru to pyridinic N (C=N–C) ratio was estimated to be 1 : 4.7 for C_3N_4–Ru–P and almost doubled to 1 : 2.0 for C_3N_4–Ru–F (Table S1†) and consistent results were obtained in ICP-MS measurements where the ruthenium content was found to increase with the amount of $RuCl_3$ added (Fig. S4†). This suggested that in the saturated structure, each Ru center was coordinated to two pyridinic nitrogen sites, as shown in the schematic diagram of Fig. 1A. In addition, the Ru : Cl ratios in both samples were very close at 1 : 0.5. Obviously, the Ru centers were not fully coordinated, which might be advantageous for catalytic reactions (*vide infra*).

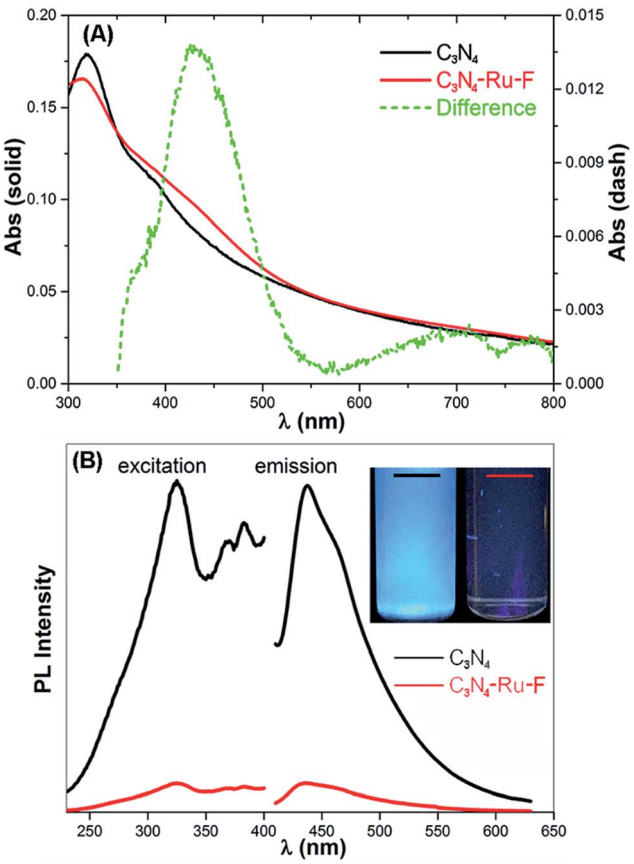

Fig. 3 (A) UV-vis spectra of C_3N_4 (black curve), C_3N_4–Ru–F (red curve) and the difference between these two spectra (green curve). (B) Photoluminescence spectra of C_3N_4 (black curve) and C_3N_4–Ru–F (red curve). Inset is the corresponding photographs of C_3N_4 and C_3N_4–Ru dispersions under 365 nm UV irradiation.

Further structural insights were obtained in UV-vis and PL measurements. From Fig. 3A, one can see that the as-prepared C_3N_4 nanosheets (black curve) exhibited an absorption peak at around 320 nm, similar to that observed with graphene quantum dots,[55,56] and a weak, broad peak at *ca.* 390 nm which can be assigned to π–π^* transitions that are commonly observed in conjugated ring systems including heterocyclic aromatics.[57] Similar optical characteristics can be seen with C_3N_4–Ru–F (red curve). However, the difference between these two spectra shows a new absorption band between 350 nm and 550 nm, where the peak at *ca.* 431 nm (green curve) is likely due to MLCT transitions, as observed previously with ruthenium–bipyridine complexes.[58,59]

Furthermore, both C_3N_4 and C_3N_4–Ru–F exhibited rather consistent PL profiles, with the emission peak (λ_{em}) at 436 nm under the excitation (λ_{ex}) of 330 nm at room temperature (Fig. 3B).[25,60] However, it can be seen that the emission intensity of C_3N_4–Ru–F decreased by about 91% as compared to that of C_3N_4, most likely because the emission coincided with the MLCT absorption of the Ru–N moieties (panel A) as well as because of marked diminishment of the C_3N_4 bandgap upon ruthenium ion complexation, as suggested in DFT calculations (*vide infra*). This is also manifested in the photographs of C_3N_4 and C_3N_4–Ru–F solutions under photoirradiation at 365 nm (Fig. 3B inset). The substantial quenching of the PL emission of C_3N_4–Ru–F, as compared to that of C_3N_4, suggested that ruthenium ion complexation suppressed radiative recombination of the photo-generated electron–hole pairs.[61,62]

The electrocatalytic activities of the samples towards HER were then evaluated by electrochemical measurements in a N_2-saturated 0.5 M H_2SO_4 solution. Fig. 4A depicts the polarization curves of the various electrocatalysts loaded onto a glassy carbon electrode. One can see that at increasingly negative potentials, nonzero currents started to emerge with C_3N_4, C_3N_4–Ru–P and C_3N_4–Ru–F, in comparison to those of the electrocatalytically inactive carbon black, indicating effective HER activity of the materials. Yet the activity varied markedly among the series. For instance, the overpotential (η_{10}) required to achieve the current density of 10 mA cm^{-2} was only −140 mV for C_3N_4–Ru–F, markedly lower than those for C_3N_4–Ru–P (−189 mV) and C_3N_4 (−296 mV). For comparison, η_{10} for Ru nanoparticles was −233 mV,[63] signifying limited activity of (metallic) ruthenium nanoparticles towards hydrogen evolution. This indicates that it is the incorporation of ruthenium metal ions into the C_3N_4 matrix that significantly enhanced the HER activity, which increased with increasing loading of the metal centers (Fig. S4†). Also, at the same overpotential of −200 mV, the current densities were the highest at 33.32 mA cm^{-2} for C_3N_4–Ru–F, as compared to 12.73 mA cm^{-2} for C_3N_4–Ru–P and 2.84 mA cm^{-2} for C_3N_4 (Fig. S5†). That is, the HER activity of C_3N_4–Ru–F is 2.6 times that of C_3N_4–Ru–P and 11.7 times that of C_3N_4. Notably, whereas the overall performance remains subpar as compared to that of state-of-the-art Pt/C (which exhibited an η_{10} of only −38 mV), it is better than the leading results of C_3N_4-based HER electrocatalysts reported in recent literature, and is comparable to those based on non-precious metals and compounds (Table S2†).

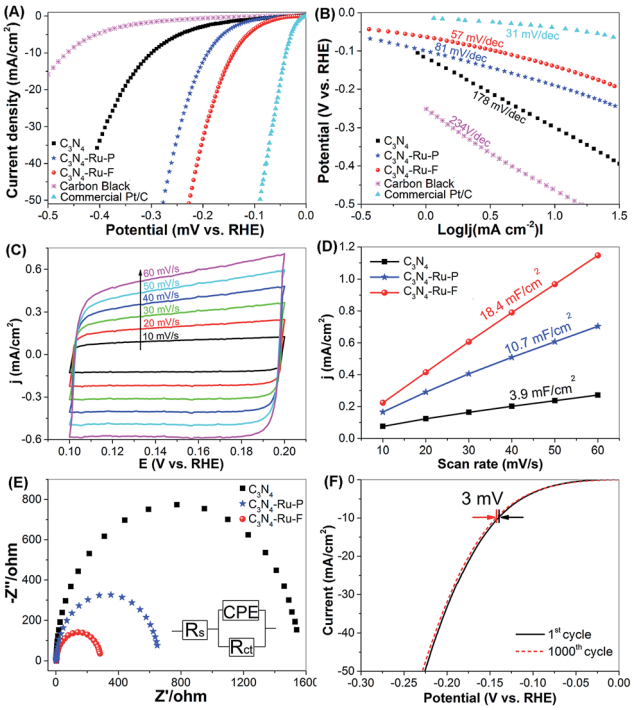

Fig. 4 (A) Polarization curves of HER on various electrocatalysts in 0.5 M H_2SO_4. (B) Corresponding Tafel plots derived from panel (A). (C) Cyclic voltammograms within the range of +0.1 to +0.2 V where no faradaic reaction occurred at difference scan rates. (D) Variation of the double-layer charging currents at +0.15 V *versus* scan rate. (E) Nyquist plots collected at the overpotential of −50 mV. Inset is the equivalent circuit of the electrocatalyst-modified electrode, where R_s is (uncompensated) resistance, R_{ct} is charge-transfer resistance and CPE is the constant-phase element (equivalent to C_{dl}). (F) The 1st and 1000th cycles of HER polarization curves on C_3N_4–Ru–F in the stability test.

Additionally, the linear portions of the polarization curves (Fig. 4B) were fitted to the Tafel equation, $\eta = a \log |j| + b$ (j is the current density and a is the Tafel slope), and the Tafel slope was estimated to be 57 mV dec^{-1} for C_3N_4–Ru–F, much lower than those for C_3N_4–Ru–P (81 mV dec^{-1}) and C_3N_4 (178 mV dec^{-1}). For comparison, the Tafel slope was *ca.* 31 mV dec^{-1} for commercial Pt/C, consistent with the results of earlier studies,[13,64] and markedly greater at 234 mV dec^{-1} for the poorly active carbon black.

Note that the HER involves three major steps, each of which carries a specific Tafel slope:

(1) Volmer reaction (Tafel slope 120 mV dec^{-1}): $H_3O^+ + e^- \rightarrow H^* + H_2O$.

(2) Heyrovsky reaction (Tafel slope 40 mV dec^{-1}): $H^* + H_3O^+ + e^- \rightarrow H_2 + H_2O$.

(3) Tafel reaction (Tafel slope 30 mV dec^{-1}): $2H^* \rightarrow H_2$

where the asterisks denote surface-adsorbed species. Based on the Tafel slopes obtained above, one can see that the rate-determining step (RDS) of HER on Pt/C is most likely the Tafel reaction where molecular hydrogen (H_2) is formed by adsorbed hydrogen (H^*) and released from the catalyst surface, due to the high activity of platinum in the reduction of proton to atomic hydrogen.[65] For the C_3N_4–Ru complexes, the HER

activity was likely dictated by the combined Volmer and Heyrovsky reactions, where the RDS involves the formation of metal–hydride moieties. Furthermore, the exchange current density (J_o) can be estimated by extrapolation of the Tafel plot to the x axis to be 0.072 mA cm^{-2} for C_3N_4–Ru–F, which is also superior/comparable to the results reported in recent literature with relevant electrocatalysts (Table S2†). For comparison, J_o was markedly lower at 0.014.5 mA cm^{-2} for C_3N_4–Ru–P, and 0.00015 mA cm^{-2} for C_3N_4, whereas much higher at 1.5 mA cm^{-2} for Pt/C.

In the above electrochemical measurements, one can clearly see that the HER activity of the as-prepared C_3N_4 nanosheets alone was very poor, markedly lower than those of the C_3N_4–Ru composites. This suggests minimal contributions of pyridinic nitrogen in C_3N_4 to hydrogen reduction, in contradiction to the results in prior studies where DFT calculations and experimental results suggested that hybrid materials based on carbon nitride and nitrogen-doped graphene might be active for HER electrocatalysis.[66,67] In the present study, the remarkable HER performance of C_3N_4–Ru is most likely due to the ruthenium metal centers embedded within the C_3N_4 matrix, where the Ru–N moieties behaved analogously to conventional metal complexes for the HER.[18,21,22] In fact, when the ruthenium metal centers were replaced by other transition-metal ions, such as Fe(III), Co(III), Ni(III), and Cu(II), the HER performance of the resulting C_3N_4-M composites diminished substantially and became comparable to that of C_3N_4 alone (Fig. S6 and S7 and Table S3†), indicating the unique role of ruthenium centers in the electroreduction of protons to hydrogen. The HER activity of C_3N_4–Ru–F was also manifested in full water splitting with commercial RuO_2 as the OER catalyst, where the amount of hydrogen generated was 2.05 times that of oxygen (Fig. S8†).

Further insights into the interactions between ruthenium metal centers and the C_3N_4 matrix were obtained by quantitative analysis of the electrochemically active surface area (ECSA) and charge-transfer resistance (R_{ct}). Fig. 4C depicts the cyclic voltammograms of C_3N_4–Ru–F recorded at different scan rates (10 to 60 mV s^{-1}) in the potential range of +0.1 to +0.2 V *vs.* RHE, where no faradaic reaction occurred (the data of C_3N_4 and C_3N_4–Ru–P are shown in Fig. S9†). Fig. 4D plotted the current density at +0.15 V *versus* the potential scan rate and the double layer capacitance (C_{dl}, which is proportional to ECSA) of C_3N_4–Ru–F was estimated to be 18.4 mF cm^{-2}, which was 4.7 times that of C_3N_4 (3.9 mF cm^{-2}), and 1.7 times that of C_3N_4–Ru–P (10.7 mF cm^{-2}). This may be ascribed to the enhanced electrical conductivity of the composites with the incorporation of metal centers into the C_3N_4 molecular skeleton. Taking into consideration the low mass loading of 0.153 mg cm^{-2} of the composites, the C_{dl} values were also comparable to results reported in prior studies (Table S2†).

Electrochemical impedance measurements were then carried out to quantify the corresponding R_{ct}. Fig. S10† depicts the typical Nyquist plots of C_3N_4–Ru–F at various overpotentials, and R_{ct} was estimated by fitting the data to Randle's equivalent circuit (inset to Fig. 4E). One can see that R_{ct} decreased significantly with increasing overpotentials. Fig. 4E compares the Nyquist plots of the various electrocatalysts at the overpotential of −50 mV, where R_{ct} was estimated to be 285 Ω for C_3N_4–Ru–F, 658 Ω for C_3N_4–Ru–P and 1550 Ω for C_3N_4. Indeed, one can see that the embedment of ruthenium metal centers within the C_3N_4 matrix greatly facilitated the electron-transfer kinetics, consistent with the results from the above voltammetric measurements.

Besides excellent electrocatalytic activity, stability of the catalysts is also an important variable in practical applications. For C_3N_4–Ru–F, the polarization profiles remained almost invariant after 1000 cycles of potential scans, with the η_{10} value increased by only 3 mV, suggesting long-term durability of the catalyst (Fig. 4F). In fact, XPS measurements showed no variation of the C 1s and Ru 3d electrons after 1000 electrochemical cycles (Fig. S11†).

To unravel the mechanistic insights involved, DFT calculations were conducted to examine the effect of the incorporation of ruthenium ions into the C_3N_4 matrix on the band structures and Gibbs free energy of hydrogen adsorption and reduction. 2 × 2 supercells of C_3N_4 and C_3N_4–Ru were used for the calculations (Fig. S12–S14†), where a ruthenium ion was bonded to two nitrogen sites, as suggested by the experimental results (Fig. 2 and Table S1†). The calculated band structure of C_3N_4 (Fig. 5A) suggests an indirect band gap of about 1.3 eV, which is in good agreement with the PDOS plot in Fig. 5B and results from previous studies.[68,69] In contrast with the semiconducting nature of C_3N_4, the band structure of C_3N_4–Ru (Fig. 5C) shows no band gap, most probably because the embedment of ruthenium ions into the C_3N_4 matrix caused a charge transfer

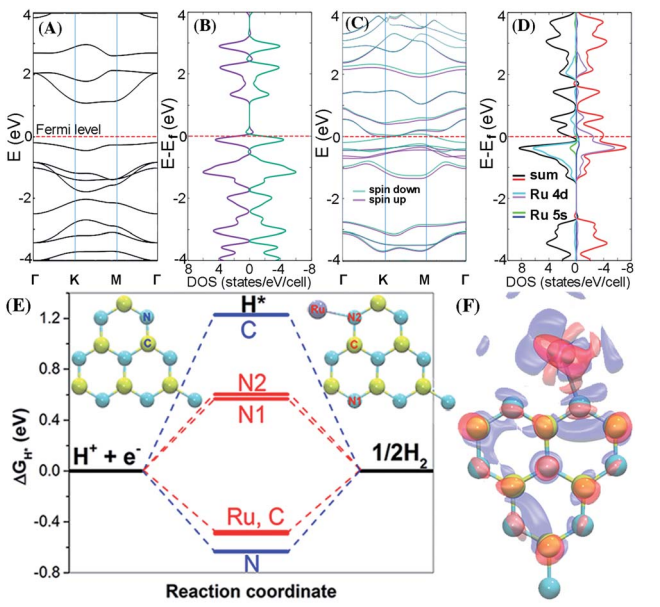

Fig. 5 (A) Band structures and (B) projected density of states of C_3N_4. (C) Band structures and (D) projected density of states of C_3N_4–Ru. Contributions of Ru 4d and 5s orbitals to the PDOS are labeled in different colors. (E) Calculated Gibbs free-energy (ΔG^*_H) of the HER at the equilibrium potential for C_3N_4 (blue) and C_3N_4–Ru (red) at various bonding sites as labeled in the panel inset. (F) Schematic of interfacial charge transfer in C_3N_4–Ru. Red signals are positive charge and blue signals are negative charge with an isosurface value of 0.003 e au^{-3}.

between C_3N_4 and ruthenium ions, as observed in XPS measurements (Fig. 2).[70] Additionally, the PDOS profile of C_3N_4–Ru shows a large density of states at the Fermi level, with the primary contributions from the Ru 4d and 5s orbitals (Fig. 5D). This indicates that the incorporation of ruthenium ions into C_3N_4 led to redistribution of the electrons within the composite, crossing of the Fermi level with the conduction band, and hence enhanced electrical conductivity, consistent with electrochemical impedance measurements (Fig. 4E). This may also explain the quenching of the C_3N_4 PL emission (Fig. 3).

Such a marked discrepancy of the electronic structures of C_3N_4–Ru, as compared to that of C_3N_4, is likely responsible for the much enhanced electrocatalytic activity of C_3N_4–Ru.[66,71,72] Notably, the HER typically involves a three-state process, an initial H^+ state, an intermediate H* state, and a $\frac{1}{2}H_2$ state as the final product (Fig. 5E); and the Gibbs free-energy of the formation of the intermediate H* state, $|\Delta G_{H^*}|$, can be used as the descriptor of the HER performance for different electrocatalysts.[73] For an ideal HER electrocatalyst, $|\Delta G_{H^*}|$ should be zero. In the present study, C_3N_4 was found to exhibit a Gibbs free energy of $\Delta G^{C}_{H^*} = +1.23$ eV and $\Delta G^{N}_{H^*} = -0.63$ eV for the carbon and nitrogen bonding sites (labeled in the left inset to Fig. 5E and S13†), respectively. Yet, when ruthenium ions were incorporated into the C_3N_4 matrix, the $|\Delta G_{H^*}|$ values were found to be substantially lower at the Ru, C, and N binding sites (labeled in the right inset to Fig. 5E and S14†), $\Delta G^{C}_{H^*} = -0.48$ eV, $\Delta G^{N1}_{H^*} = +0.57$ eV, $\Delta G^{N2}_{H^*} = +0.60$ eV and $\Delta G^{Ru}_{H^*} = -0.49$ eV (Table S4†), suggesting enhanced hydrogen adsorption by ruthenium ion complexation to C_3N_4. This is also manifested in Fig. 5F, which depicts the interfacial charge transfer between C_3N_4 and ruthenium ions (by computing the charge density difference between C_3N_4–Ru and C_3N_4 + isolated Ru atom) and the resulting charge redistribution among the entire cell. From these studies, one can see that the incorporation of ruthenium ions into the C_3N_4 molecular skeleton drastically enhanced the electrical conductivity, and facilitated the adsorption of hydrogen to various binding sites in the composites, which is likely responsible for the enhanced HER performance (Fig. S14†).

Conclusions

In this study, a new type of HER electrocatalyst was designed and synthesized by thermal refluxing of graphitic C_3N_4 nanosheets and $RuCl_3$ in water, leading to the formation of C_3N_4–Ru hybrids that exhibited apparent HER activity in acidic media. In fact, their HER activity was found to increase with increasing loading of the ruthenium ions in the C_3N_4 matrix, and the best sample displayed an overpotential of only 140 mV to achieve the current density of 10 mA cm^{-2}, a Tafel slope of 57 mV dec^{-1} and an exchange current density of 0.072 mA cm^{-2}, which is comparable/superior to results reported in recent literature with relevant HER electrocatalysts. Such a remarkable performance was ascribed to the formation of Ru–N_2 moieties that facilitated the adsorption of hydrogen, a critical step in HER catalysis, as confirmed by studies based on DFT calculations. Significantly, the results suggest that graphitic C_3N_4 nanosheets may be exploited as a unique functional scaffold for the fabrication of a wide range of single atom-like catalysts for diverse applications.[74,75]

Acknowledgements

This work was supported in part by a grant from the National Science Foundation (DMR-1409396 and CHE-1710408). XPS and TEM work was done at the Molecular Foundry and National Center for Electron Microscopy, Lawrence Berkeley National Laboratory which is supported by the US Department of Energy. This work used the Extreme Science and Engineering Discovery Environment (XSEDE), which is supported by National Science Foundation (ACI-1548562). Y. P. acknowledges start-up support from the University of California, Santa Cruz.

References

1 J. Greeley, T. F. Jaramillo, J. Bonde, I. B. Chorkendorff and J. K. Nørskov, *Nat. Mater.*, 2006, **5**, 909–913.
2 D. Voiry, H. Yamaguchi, J. Li, R. Silva, D. C. B. Alves, T. Fujita, M. Chen, T. Asefa, V. B. Shenoy and G. Eda, *Nat. Mater.*, 2013, **12**, 850–855.
3 M. Cabán-Acevedo, M. L. Stone, J. R. Schmidt, J. G. Thomas, Q. Ding, H.-C. Chang, M.-L. Tsai, J.-H. He and S. Jin, *Nat. Mater.*, 2015, **14**, 1245–1251.
4 M. G. Walter, E. L. Warren, J. R. McKone, S. W. Boettcher, Q. Mi, E. A. Santori and N. S. Lewis, *Chem. Rev.*, 2010, **110**, 6446–6473.
5 P. Du and R. Eisenberg, *Energy Environ. Sci.*, 2012, **5**, 6012–6021.
6 C. C. L. McCrory, S. Jung, I. M. Ferrer, S. M. Chatman, J. C. Peters and T. F. Jaramillo, *J. Am. Chem. Soc.*, 2015, **137**, 4347–4357.
7 S. J. A. Moniz, S. A. Shevlin, D. J. Martin, Z.-X. Guo and J. Tang, *Energy Environ. Sci.*, 2015, **8**, 731–759.
8 B. E. Conway and B. V. Tilak, *Electrochim. Acta*, 2002, **47**, 3571–3594.
9 H. I. Karunadasa, E. Montalvo, Y. Sun, M. Majda, J. R. Long and C. J. Chang, *Science*, 2012, **335**, 698–702.
10 J. Kibsgaard, Z. Chen, B. N. Reinecke and T. F. Jaramillo, *Nat. Mater.*, 2012, **11**, 963–969.
11 B. Cao, G. M. Veith, J. C. Neuefeind, R. R. Adzic and P. G. Khalifah, *J. Am. Chem. Soc.*, 2013, **135**, 19186–19192.
12 W.-F. Chen, J. T. Muckerman and E. Fujita, *Chem. Commun.*, 2013, **49**, 8896–8909.
13 E. J. Popczun, J. R. McKone, C. G. Read, A. J. Biacchi, A. M. Wiltrout, N. S. Lewis and R. E. Schaak, *J. Am. Chem. Soc.*, 2013, **135**, 9267–9270.
14 Y. Yan, B. Xia, Z. Xu and X. Wang, *ACS Catal.*, 2014, **4**, 1693–1705.
15 Y. Jiao, Y. Zheng, M. Jaroniec and S. Z. Qiao, *Chem. Soc. Rev.*, 2015, **44**, 2060–2086.
16 X. Zou and Y. Zhang, *Chem. Soc. Rev.*, 2015, **44**, 5148–5180.
17 D. Voiry, J. Yang and M. Chhowalla, *Adv. Mater.*, 2016, **28**, 6197–6206.

18 X. Hu, B. S. Brunschwig and J. C. Peters, *J. Am. Chem. Soc.*, 2007, **129**, 8988–8998.
19 P. A. Jacques, V. Artero, J. Pecaut and M. Fontecave, *Proc. Natl. Acad. Sci. U. S. A.*, 2009, **106**, 20627–20632.
20 A. Koca, *Electrochem. Commun.*, 2009, **11**, 838–841.
21 S. W. Kohl, L. Weiner, L. Schwartsburd, L. Konstantinovski, L. J. W. Shimon, Y. Ben-David, M. A. Iron and D. Milstein, *Science*, 2009, **324**, 74–77.
22 L. L. Dempsey, B. S. Brunschwig, J. R. Winkler and H. B. Gray, *Acc. Chem. Res.*, 2009, **42**, 1995–2004.
23 X. Wang, K. Maeda, A. Thomas, K. Takanabe, G. Xin, J. M. Carlsson, K. Domen and M. Antonietti, *Nat. Mater.*, 2009, **8**, 76–80.
24 J. Liang, Y. Zheng, J. Chen, J. Liu, D. Hulicova Jurcakova, M. Jaroniec and S. Z. Qiao, *Angew. Chem.*, 2012, **124**, 3958–3962.
25 Y. Wang, X. Wang and M. Antonietti, *Angew. Chem., Int. Ed.*, 2012, **51**, 68–89.
26 Y. Zheng, J. Liu, J. Liang, M. Jaroniec and S. Z. Qiao, *Energy Environ. Sci.*, 2012, **5**, 6717–6731.
27 S. Yang, Y. Gong, J. Zhang, L. Zhan, L. Ma, Z. Fang, R. Vajtai, X. Wang and P. M. Ajayan, *Adv. Mater.*, 2013, **25**, 2452–2456.
28 D. J. Martin, K. Qiu, S. A. Shevlin, A. D. Handoko, X. Chen, Z. Guo and J. Tang, *Angew. Chem., Int. Ed.*, 2014, **53**, 9240–9245.
29 H. Shi, G. Chen, C. Zhang and Z. Zou, *ACS Catal.*, 2014, **4**, 3637–3643.
30 R. Kuriki, K. Sekizawa, O. Ishitani and K. Maeda, *Angew. Chem., Int. Ed.*, 2015, **54**, 2406–2409.
31 H. Li, S. Gan, H. Wang, D. Han and L. Niu, *Adv. Mater.*, 2015, **27**, 6906–6913.
32 J. Liu, Y. Liu, N. Liu, Y. Han, X. Zhang, H. Huang, Y. Lifshitz, S.-T. Lee, J. Zhong and Z. Kang, *Science*, 2015, **347**, 970–974.
33 J. Liu, H. Wang and M. Antonietti, *Chem. Soc. Rev.*, 2016, **45**, 2308–2326.
34 H. Yu, L. Shang, T. Bian, R. Shi, G. I. N. Waterhouse, Y. Zhao, C. Zhou, L.-Z. Wu, C.-H. Tung and T. Zhang, *Adv. Mater.*, 2016, **28**, 5080–5086.
35 D. Guo, R. Shibuya, C. Akiba, S. Saji, T. Kondo and J. Nakamura, *Science*, 2016, **351**, 361–365.
36 H. Zhang, Z. Ma, J. Duan, H. Liu, G. Liu, T. Wang, K. Chang, M. Li, L. Shi, X. Meng, K. Wu and J. Ye, *ACS Nano*, 2016, **10**, 684–694.
37 J. P. Paraknowitsch, J. Zhang, D. Su, A. Thomas and M. Antonietti, *Adv. Mater.*, 2010, **22**, 87–92.
38 Y. Wang, Y. Di, M. Antonietti, H. R. Li, X. F. Chen and X. C. Wang, *Chem. Mater.*, 2010, **22**, 5119–5121.
39 Y. Wang, H. R. Li, J. Yao, X. C. Wang and M. Antonietti, *Chem. Sci.*, 2011, **2**, 446–450.
40 J. D. Hong, X. Y. Xia, Y. S. Wang and R. Xu, *J. Mater. Chem.*, 2012, **22**, 15006–15012.
41 T. Y. Ma, J. Ran, S. Dai, M. Jaroniec and S. Z. Qiao, *Angew. Chem., Int. Ed.*, 2015, **54**, 4646–4650.
42 S. E. Guo, Z. P. Deng, M. X. Li, B. J. Jiang, C. G. Tian, Q. J. Pan and H. G. Fu, *Angew. Chem., Int. Ed.*, 2016, **55**, 1830–1834.
43 J. Tian, Q. Liu, C. Ge, Z. Xing, A. M. Asiri, A. O. Al-Youbi and X. Sun, *Nanoscale*, 2013, **5**, 8921–8924.
44 X. Zhang, X. Xie, H. Wang, J. Zhang, B. Pan and Y. Xie, *J. Am. Chem. Soc.*, 2013, **135**, 18–21.
45 P. Giannozzi, S. Baroni, N. Bonini, M. Calandra, R. Car, C. Cavazzoni, D. Ceresoli, G. L. Chiarotti, M. Cococcioni, I. Dabo, A. Dal Corso, S. de Gironcoli, S. Fabris, G. Fratesi, R. Gebauer, U. Gerstmann, C. Gougoussis, A. Kokalj, M. Lazzeri, L. Martin-Samos, N. Marzari, F. Mauri, R. Mazzarello, S. Paolini, A. Pasquarello, L. Paulatto, C. Sbraccia, S. Scandolo, G. Sclauzero, A. P. Seitsonen, A. Smogunov, P. Umari and R. M. Wentzcovitch, *J. Phys.: Condens. Matter*, 2009, **21**, 395502.
46 K. F. Garrity, J. W. Bennett, K. M. Rabe and D. Vanderbilt, *Comput. Mater. Sci.*, 2014, **81**, 446–452.
47 N. Marzari, D. Vanderbilt, A. De Vita and M. C. Payne, *Phys. Rev. Lett.*, 1999, **82**, 3296–3299.
48 S. Baroni, S. de Gironcoli, A. Dal Corso and P. Giannozzi, *Rev. Mod. Phys.*, 2001, **73**, 515–562.
49 Y. Wang, H. Li, J. Yao, X. Wang and M. Antonietti, *Chem. Sci.*, 2011, **2**, 446–450.
50 E. T. Kang, K. G. Neoh, S. H. Khor, K. L. Tan and B. T. G. Tan, *Polymer*, 1990, **31**, 202–207.
51 S. I. Orysyk, L. N. Rybachuk, V. I. Pekhnyo, A. M. Korduban and T. M. Buslaeva, *Russ. J. Inorg. Chem.*, 2010, **55**, 1075–1082.
52 C. Agnès, J.-C. Arnault, F. Omnès, B. Jousselme, M. Billon, G. Bidan and P. Mailley, *Phys. Chem. Chem. Phys.*, 2009, **11**, 11647–11654.
53 C. Creutz and N. Sutin, *Proc. Natl. Acad. Sci. U. S. A.*, 1975, **72**, 2858–2862.
54 V. Q. Nguyen, X. N. Sun, F. Lafolet, J. F. Audibert, F. Miomandre, G. Lemercier, F. Loiseau and J. C. Lacroix, *J. Am. Chem. Soc.*, 2016, **138**, 9381–9384.
55 D. Pan, J. Zhang, Z. Li and M. Wu, *Adv. Mater.*, 2010, **22**, 734–738.
56 Y. Li, Y. Hu, Y. Zhao, G. Shi, L. Deng, Y. Hou and L. Qu, *Adv. Mater.*, 2011, **23**, 776–780.
57 A. B. Jorge, D. J. Martin, M. T. S. Dhanoa, A. S. Rahman, N. Makwana, J. Tang, A. Sella, F. Corà, S. Firth, J. A. Darr and P. F. McMillan, *J. Phys. Chem. C*, 2013, **117**, 7178–7185.
58 B. S. Howerton, D. K. Heidary and E. C. Glazer, *J. Am. Chem. Soc.*, 2012, **134**, 8324–8327.
59 M. R. Norris, J. J. Concepcion, C. R. K. Glasson, Z. Fang, A. M. Lapides, D. L. Ashford, J. L. Templeton and T. J. Meyer, *Inorg. Chem.*, 2013, **52**, 12492–12501.
60 A. Thomas, A. Fischer, F. Goettmann, M. Antonietti, J. O. Muller, R. Schlogl and J. M. Carlsson, *J. Mater. Chem.*, 2008, **18**, 4893–4908.
61 Z. Ding, X. Chen, M. Antonietti and X. Wang, *ChemSusChem*, 2011, **4**, 274–281.
62 J. Zhang, M. Zhang, C. Yang and X. Wang, *Adv. Mater.*, 2014, **26**, 4121–4126.
63 R. K. Shervedani and A. Amini, *Carbon*, 2015, **93**, 762–773.
64 Y. Li, H. Wang, L. Xie, Y. Liang, G. Hong and H. Dai, *J. Am. Chem. Soc.*, 2011, **133**, 7296–7299.

65 L. J. Yang, W. J. Zhou, J. Lu, D. M. Hou, Y. T. Ke, G. Q. Li, Z. H. Tang, X. W. Kang and S. W. Chen, *Nano Energy*, 2016, **22**, 490–498.
66 Y. Zheng, Y. Jiao, Y. Zhu, L. H. Li, Y. Han, Y. Chen, A. Du, M. Jaroniec and S. Z. Qiao, *Nat. Commun.*, 2014, **5**, 3783.
67 Y. Zhao, F. Zhao, X. Wang, C. Xu, Z. Zhang, G. Shi and L. Qu, *Angew. Chem., Int. Ed.*, 2014, **53**, 13934–13939.
68 X. Li, Y. Dai, Y. Ma, S. Han and B. Huang, *Phys. Chem. Chem. Phys.*, 2014, **16**, 4230–4235.
69 X. C. Wang, K. Maeda, A. Thomas, K. Takanabe, G. Xin, J. M. Carlsson, K. Domen and M. Antonietti, *Nat. Mater.*, 2009, **8**, 76–80.
70 H.-W. Zuo, C.-H. Lu, Y.-R. Ren, Y. Li, Y.-F. Zhang and W.-K. Chen, *Acta Phys.-Chim. Sin.*, 2016, **32**, 1183–1190.
71 H. Li, C. Tsai, A. L. Koh, L. L. Cai, A. W. Contryman, A. H. Fragapane, J. H. Zhao, H. S. Han, H. C. Manoharan, F. Abild-Pedersen, J. K. Norskov and X. L. Zheng, *Nat. Mater.*, 2016, **15**, 48–53.
72 Z. F. Huang, J. Song, K. Li, M. Tahir, Y. T. Wang, L. Pan, L. Wang, X. Zhang and J. J. Zou, *J. Am. Chem. Soc.*, 2016, **138**, 1359–1365.
73 J. K. Norskov, T. Bligaard, A. Logadottir, J. R. Kitchin, J. G. Chen, S. Pandelov and J. K. Norskov, *J. Am. Chem. Soc.*, 2005, **152**, J23–J26.
74 S. X. Liang, C. Hao and Y. T. Shi, *Chemcatchem*, 2015, **7**, 2559–2567.
75 X. F. Yang, A. Q. Wang, B. T. Qiao, J. Li, J. Y. Liu and T. Zhang, *Acc. Chem. Res.*, 2013, **46**, 1740–1748.

Journal of Materials Chemistry A

CORRECTION

Correction: Hydrogen evolution reaction catalyzed by ruthenium ion-complexed graphitic carbon nitride nanosheets

Cite this: DOI: 10.1039/c7ta90195j

Yi Peng,[a] Bingzhang Lu,[a] Limei Chen,[a] Nan Wang,[b] Jia En Lu,[a] Yuan Ping*[a] and Shaowei Chen*[a]

DOI: 10.1039/c7ta90195j

www.rsc.org/MaterialsA

Correction for 'Hydrogen evolution reaction catalyzed by ruthenium ion-complexed graphitic carbon nitride nanosheets' by Yi Peng *et al.*, *J. Mater. Chem. A*, 2017, DOI: 10.1039/c7ta03826g.

The authors regret the incorrect labelling of Fig. 2. The correct version is shown below.

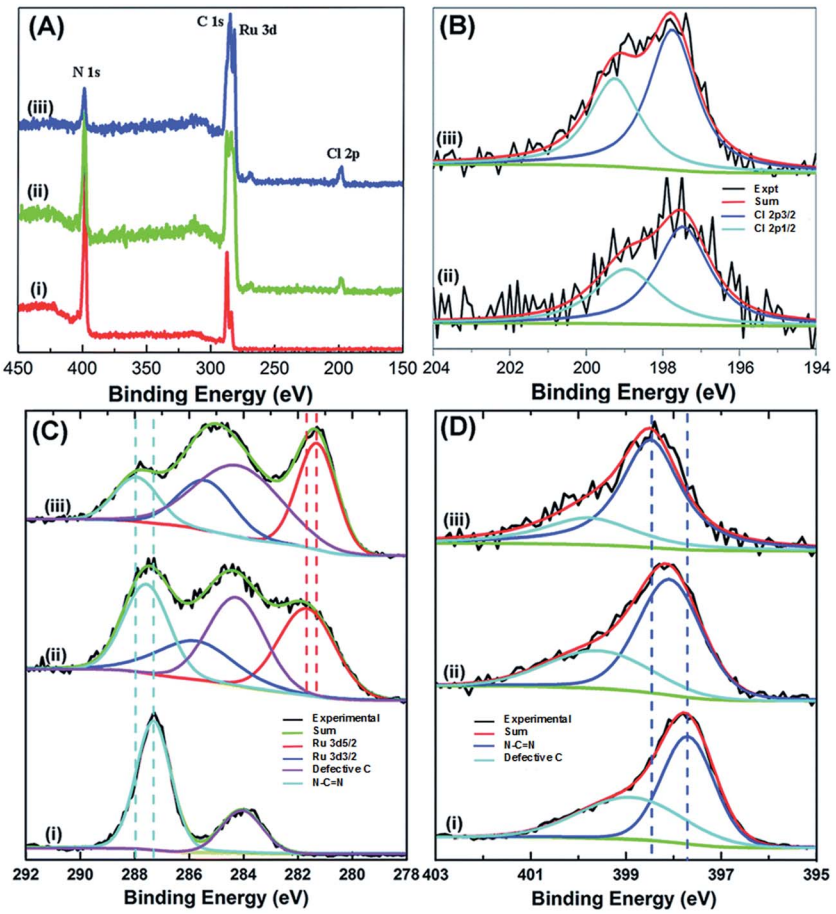

Fig. 2 (A) XPS survey spectra of (i) C_3N_4, (ii) C_3N_4–Ru–P, and (iii) C_3N_4–Ru–F. High-resolution XPS spectra of (B) Cl 2p, (C) C 1s and Ru 3d, and (D) N 1s electrons. Black curves are experimental data and colored curves are deconvolution fits.

The Royal Society of Chemistry apologises for these errors and any consequent inconvenience to authors and readers.

[a]*Department of Chemistry and Biochemistry, University of California, 1156 High Street, Santa Cruz, CA 95064, USA. E-mail: shaowei@ucsc.edu*

[b]*New Energy Research Institute, School of Environment and Energy, South China University of Technology, Guangzhou High Education Mega Centre, Guangzhou, Guangdong 510006, China*